

ARTICLE

Open Access

High spin mixing conductance and spin interface transparency at the interface of a $\text{Co}_2\text{Fe}_{0.4}\text{Mn}_{0.6}\text{Si}$ Heusler alloy and Pt

Braj Bhusan Singh¹, Koustuv Roy¹, Pushpendra Gupta¹, Takeshi Seki^{2,3}, Koki Takanashi^{2,3,4} and Subhankar Bedanta¹

Abstract

Ferromagnetic materials exhibiting low magnetic damping (α) and moderately high-saturation magnetization are required from the viewpoints of generation, transmission, and detection of spin waves. Since spin-to-charge conversion efficiency is another important parameter, high spin mixing conductance ($g_r^{\uparrow\downarrow}$) is the key for efficient spin-to-charge conversion. Full Heusler alloys, e.g., $\text{Co}_2\text{Fe}_{0.4}\text{Mn}_{0.6}\text{Si}$ (CFMS), which are predicted to be 100% spin-polarized, exhibit low α . However, $g_r^{\uparrow\downarrow}$ at the interface between CFMS and a paramagnet is not fully understood. Here, we report investigations of spin pumping and the inverse spin Hall effect in CFMS/Pt bilayers. Damping analysis indicates the presence of significant spin pumping at the interface of CFMS and Pt, which is also confirmed by the detection of an inverse spin Hall voltage. We show that in CFMS/Pt, $g_r^{\uparrow\downarrow}$ ($1.70 \times 10^{20} \text{ m}^{-2}$) and the interface transparency (83%) are higher than the values reported for other ferromagnetic/heavy metal systems. We observed a spin Hall angle of ~ 0.026 for the CFMS/Pt bilayer system.

Introduction

Spin transport across interfaces in ferromagnetic (FM)/heavy metal (HM) systems is important to develop future spintronic devices^{1,2}. Spin orbital torque³, spin-transfer torque^{1,2}, the spin pumping/inverse spin Hall effect^{4,5}, spin Seebeck effects⁶, etc. are major phenomena that are predominantly affected by interface spin transport in FM/HM systems. Spin pumping is an efficient method to produce pure spin current (\vec{J}_s), which is the flow of spin angular momentum, and investigate spin propagation across FM/HM interfaces. The efficiency of spin transport at FM/HM interfaces is characterized by a factor known as the spin mixing conductance ($g_r^{\uparrow\downarrow}$), which is related to

\vec{J}_s by the expression²

$$\vec{J}_s = \frac{\hbar}{4\pi} g_r^{\uparrow\downarrow} \hat{m} \times \frac{d\hat{m}}{dt}, \quad (1)$$

where \hat{m} is the unit vector of magnetization. \vec{J}_s can be converted into the transverse voltage (V_{ISHE}) by the inverse spin Hall effect (ISHE)⁷:

$$V_{\text{ISHE}} \propto \theta_{\text{SH}} \left| \vec{J}_s \times \vec{\sigma} \right|, \quad (2)$$

where θ_{SH} is the spin Hall angle, which defines the conversion efficiency between the charge current (\vec{J}_c) and \vec{J}_s , and $\vec{\sigma}$ contains the spin matrices governed by the spin-polarization direction. Therefore, in order to obtain high V_{ISHE} and hence $g_r^{\uparrow\downarrow}$ in an FM/HM heterostructure, θ_{SH} of the HM needs to be large. The value of θ_{SH} depends mostly on the spin-orbit interaction (SOI) and conductivity of the HM^{2,8}. Efficient interfacial spin transport critically depends on the type of interfaces and its associated FM and HM materials, and FM materials with

Correspondence: Subhankar Bedanta (sbedanta@niser.ac.in)

¹Laboratory for Nanomagnetism and Magnetic Materials (LNMM), School of Physical Sciences, National Institute of Science Education and Research (NISER), HBNI, Jatni, Odisha, India

²Institute for Materials Research, Tohoku University, Sendai, Japan
Full list of author information is available at the end of the article

© The Author(s) 2021

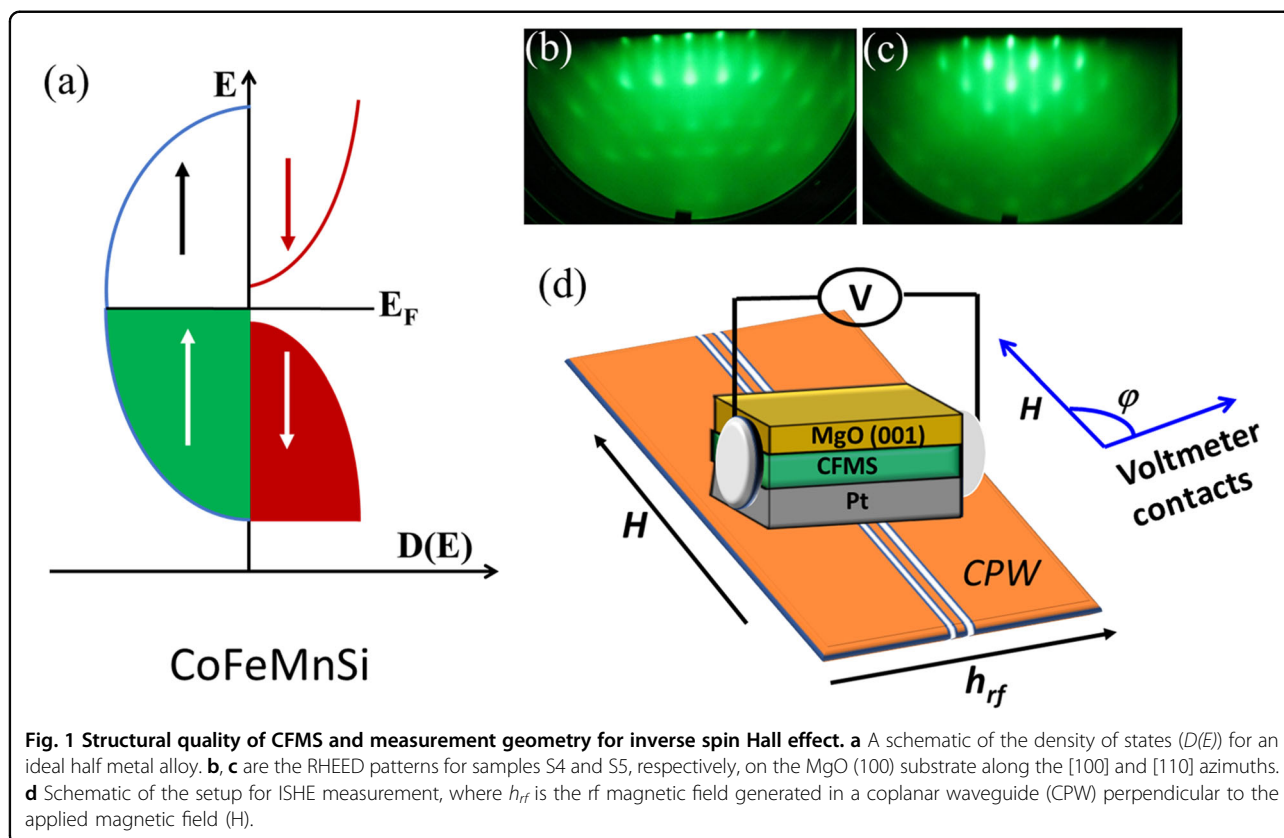
 **Open Access** This article is licensed under a Creative Commons Attribution 4.0 International License, which permits use, sharing, adaptation, distribution and reproduction in any medium or format, as long as you give appropriate credit to the original author(s) and the source, provide a link to the Creative Commons license, and indicate if changes were made. The images or other third party material in this article are included in the article's Creative Commons license, unless indicated otherwise in a credit line to the material. If material is not included in the article's Creative Commons license and your intended use is not permitted by statutory regulation or exceeds the permitted use, you will need to obtain permission directly from the copyright holder. To view a copy of this license, visit <http://creativecommons.org/licenses/by/4.0/>.

low magnetic damping (α) are important to generate large spin currents and hence high $g_r^{\uparrow\downarrow}$. In this context, various low-damping materials, such as NiFe, CoFeB, and $Y_3Fe_5O_{12}$, have been studied. Further, there is another class of half-metallic materials, e.g., Heusler alloys, which have been established as low-damping systems. It is also noted here that spin pumping and the resultant spin current can be described as an accumulation of up and down spins⁹. Therefore, it is expected that the spin pumping efficiency is larger in Heusler alloys than in other alloys due to the presence of only one type of spin at the Fermi level. In addition, low magnetic damping and expected high spin pumping make Heusler alloys suitable for interface spin transport studies and pure spin current-based spin-torque nano-oscillators¹⁰. There have been intense studies of spin dynamics with low-damping materials, e.g., NiFe and CoFeB with various HMs^{11–15}. However, there are only a few reports on the spin dynamics of Heusler alloys with HMs^{9,16}. $Co_2Fe_{0.4}Mn_{0.6}Si$ (CFMS) is a Heusler alloy that shows low damping and 100% spin polarization¹⁷. Figure 1a shows a typical schematic for the density of states for a half-metallic material. However, $g_r^{\uparrow\downarrow}$ in CFMS/HM systems has so far not been evaluated, which would help to understand their use for applications. Here, we report on a spin pumping study in a CFMS/Pt system with varying Pt thickness via

(1) measurement of the ISHE, (2) evaluation of $g_r^{\uparrow\downarrow}$ and (3) and characterization of the spin interface transparency.

Materials and methods

The bilayer samples *viz.* S1# CFMS(20 nm)/Pt(3 nm), S2# CFMS(20 nm)/Pt(5 nm), S3# CFMS(20 nm)/Pt(7 nm), S4# CFMS(20 nm)/Pt(10 nm), S5# CFMS(20 nm)/Pt(20 nm), and S6# CFMS(20 nm) were prepared on MgO (100) substrates using dc magnetron sputtering in a vacuum system with a base pressure of $\sim 1 \times 10^{-9}$ mbar¹⁸. The composition of CFMS was $Co_2Fe_{0.4}Mn_{0.6}Si$. This composition was chosen due to the observation of the lowest α at 60% Mn concentration in a recent study by Pan et al.¹⁹. The prepared CFMS thin films were annealed in situ at 600 °C/1 h to improve their crystallinity and surface quality. Reflection high-energy electron diffraction (RHEED) patterns were acquired to characterize the surface and crystalline quality of the CFMS layers. After the preparation of the CFMS layer, the Pt layer was deposited at room temperature by dc magnetron sputtering. The thickness and interface roughness of the films were evaluated using X-ray reflectivity (XRR) as measured by an X-ray diffractometer (Rigaku Smartlab). Ferromagnetic resonance (FMR) measurements have been performed in the frequency range of 5–17 GHz on a coplanar waveguide in the flip-chip manner^{20,21}.



ISHE measurements were performed by connecting a nanovoltmeter over two ends of the sample (sample size: 3×2 mm). The details of the ISHE setup can be found elsewhere²².

Results and discussion

Crystalline quality

Figure 1b, c shows the RHEED patterns for samples S4 and S5, respectively, observed along the MgO[100] and MgO[110] azimuths. From the streaks and spots of the RHEED patterns, it is confirmed that a CFMS layer with a (001) crystalline orientation was epitaxially grown on the MgO (001) substrate. The streak lines that are elongated spots in the vertical direction in the RHEED pattern imply the improvement of flatness at the CFMS surface. Supplementary Fig. A1 in the Supplementary Information shows the XRR data and the corresponding best fits. From the best fits, the values of interface roughness at the CFMS-Pt interface are found to be 0.9 ± 0.02 , 1.0 ± 0.02 , 1.4 ± 0.03 , 1.4 ± 0.03 , 1.4 ± 0.03 , and 1.5 ± 0.02 nm for samples S1–S5. Figure 1d shows the sample structure and ISHE measurement geometry, which are discussed in the next section.

Magnetic damping

Figure 2a, b shows the plots of resonance frequency (f) versus resonance field (H_r) and linewidth (ΔH) versus f , respectively. Here, the values of H_r and ΔH were evaluated using FMR spectra (see Supplementary Fig. A2a, b for samples S1 and S5, respectively, in the Supplementary Information). To evaluate the gyromagnetic ratio (γ) and effective demagnetization ($4\pi M_{eff}$), Fig. 2a was fitted to Kittel's equation²³ as:

$$f = \frac{\gamma}{2\pi} \sqrt{(H_K + H_r)(H_K + H_r + 4\pi M_{eff})}, \quad (3)$$

where

$$4\pi M_{eff} = 4\pi M_s + \frac{2K_s}{M_s t_{FM}} \quad (4)$$

and H_K , K_s , M_s , and t_{FM} are the anisotropy field, perpendicular surface magnetic anisotropy constant, saturation magnetization, and thickness of the FM layer, respectively. Here, α was evaluated by fitting the data of Fig. 2b using the following expression²⁴:

$$\Delta H = \Delta H_0 + \frac{4\pi\alpha f}{\gamma}, \quad (5)$$

where ΔH_0 is the inhomogeneous broadening of the linewidth, which depends on the homogeneity of the sample. There are various other effects, such as interface

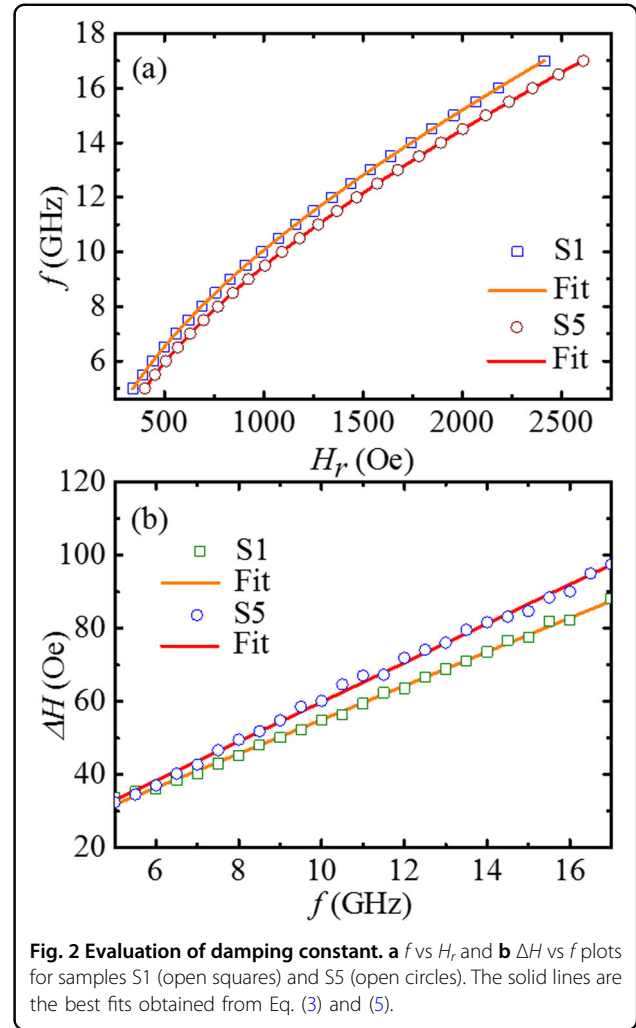


Fig. 2 Evaluation of damping constant. **a** f vs H_r and **b** ΔH vs f plots for samples S1 (open squares) and S5 (open circles). The solid lines are the best fits obtained from Eq. (3) and (5).

effects, impurities, and magnetic proximity effects (MPEs), which can also enhance the value of α of the system. Hence, the total α can be written as:

$$\alpha = \alpha_{\text{int}} + \alpha_{\text{impurity}} + \alpha_{\text{MPE}} + \alpha_{\text{sp}}, \quad (6)$$

where α_{int} is the intrinsic damping. Further α_{impurity} , α_{MPE} , and α_{sp} are the contributions from impurities, MPE, and spin pumping to α , respectively²⁵.

The linear behavior of the ΔH vs f plots implies good homogeneity in our samples. It is observed from Table 1 that Sample S2 shows the lowest value of ΔH_0 , which indicates better homogeneity in the sample. Further, S2 shows the highest spin pumping voltage among all samples, which is discussed later. However, sample S3 shows the highest value of ΔH_0 among all samples, which indicates a more disordered structure in S3. We also observed a negative sign of H_K for samples S1 and S5. This may be due to the orientation of the sample with respect to the magnetic field direction in the FMR setup.

Table 1 Parameters extracted by fitting the experimental data to Eqs (3) and (5) of the main text.

Sample	γ (GHz/Oe)	$4\pi M_{eff}$ (Oe)	H_K (Oe)	ΔH_0 (Oe)
S1	0.0185	12206 ± 8	-110 ± 1	9.7 ± 0.3
S2	0.0185	11181 ± 32	122 ± 2	2.9 ± 0.2
S3	0.0185	11181 ± 69	78 ± 1	17.8 ± 2.0
S4	0.0185	11323 ± 28	118 ± 2	3.0 ± 0.8
S5	0.0185	11180 ± 24	-146 ± 2	3.5 ± 0.2
S6	0.0185	12336 ± 18	-105 ± 2	15.3 ± 0.7

Table 2 The values of α for samples S1–S6.

S1	0.0066 ± 0.0001
S2	0.0063 ± 0.0001
S3	0.0070 ± 0.0001
S4	0.0085 ± 0.0001
S5	0.0087 ± 0.0001
S6	0.0048 ± 0.0001

We have observed this change in sign while performing in-plane angle-dependent damping measurements; the sign changes from $-ve$ to $+ve$ after 180° rotation.

From Table 2, it is observed that the values of α for the bilayer samples (S1–S5) are larger than the value for a single layer of CFMS (S6). See Supplementary Fig. A3 a, b in the Supplementary Information showing the frequency-dependent resonance and linewidth, respectively. The best fit to Supplementary Fig. A3b yields an α value for sample S6 of $\sim 0.0048 \pm 0.0001$, which is consistent with the reported value in the literature¹⁸. This enhancement in the values of α is an indication of spin pumping. However, we cannot rule out other effects, e.g., MPE, and any impurities that may contribute to enhancing the value of α (see Eq. (6)). To investigate the MPE or magnetic dead layer formation at the interface, we measured the M_s for all the samples by a SQUID magnetometer (data not shown). The measured values of M_s for all the samples were found to be 861 emu/cc (S1), 842 emu/cc (S2), 792 emu/cc (S3), 845 emu/cc (S4), and 807 emu/cc (S5).

Inverse spin Hall effect measurement

To confirm the spin pumping in our system, we performed ISHE measurements on all the samples, as shown in schematic Fig. 1d. The measurements are carried out at +15 dBm power and 7 GHz frequency.

The angle φ denotes the angle between the measured voltage direction and the perpendicular direction of the

applied DC magnetic field (H). Angle-dependent measurements of the voltage were conducted to identify and remove spin rectification effects, e.g., anisotropic magnetoresistance (AMR) and the anomalous Hall effect (AHE). Figure 3 shows the measured voltage (V_{meas}) (open blue symbol) versus H along with the FMR signal (open black symbol) for sample S1 at angles $\varphi = 0^\circ$ (a), 30° (b), 90° (c), and 180° (d). It should be noted that $\varphi = 0^\circ$ means that the field was applied along the easy-magnetization axis of the sample. There was a very weak signal observed at $\varphi = 90^\circ$ (Fig. 3b). This is due to the negligible amount of spin accumulation parallel to the applied magnetic field. It is evident from Fig. 3a, d that the sign of V_{meas} is reversed when φ moves from 0° to 180° . This indicates that the voltage is produced primarily by spin pumping. It is well-known that if the sign of V_{meas} does not reverse with the angle, then the contribution comes solely from different spin rectification effects.

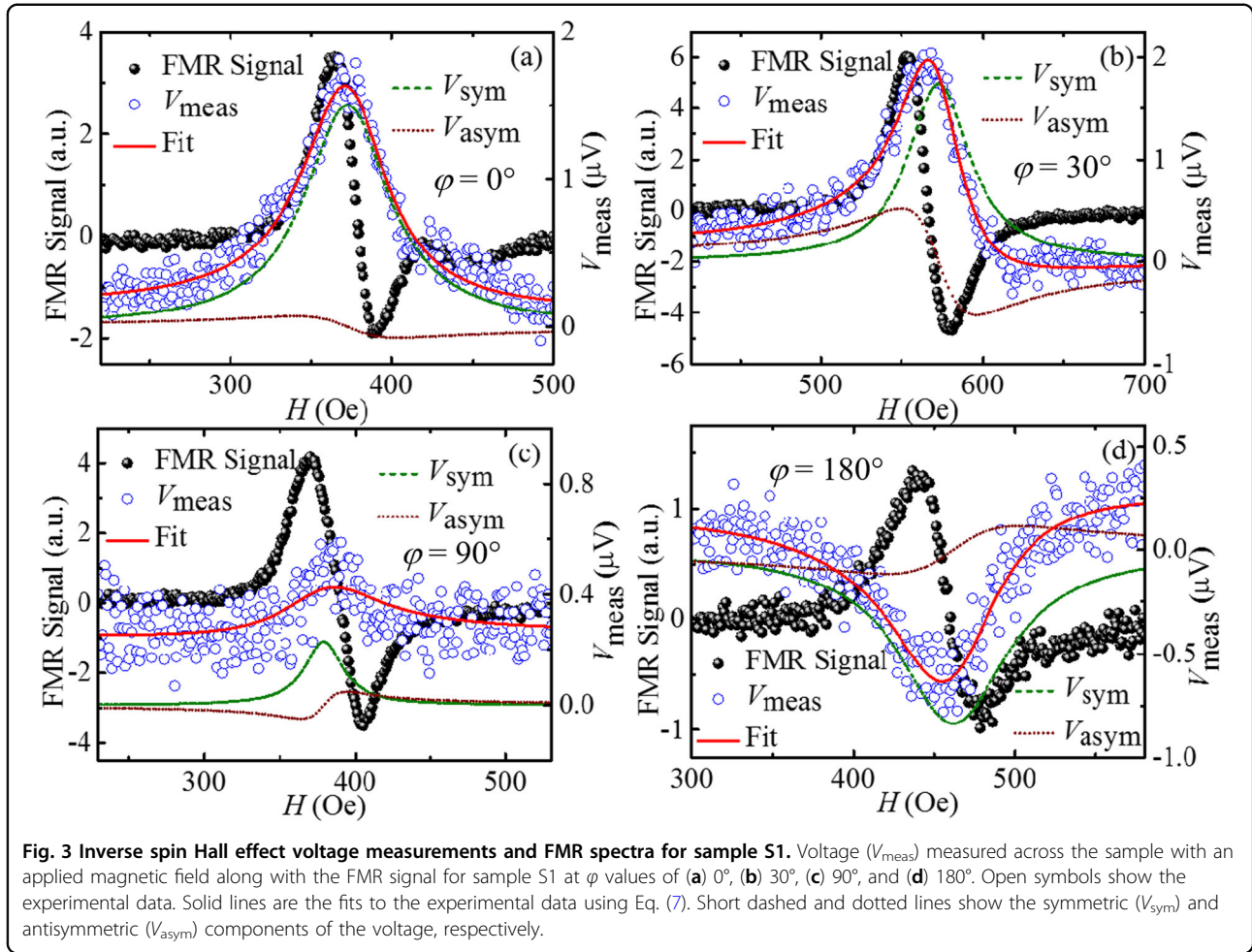
Figure 4 shows a V_{meas} versus H plot for sample S5 measured at $\varphi = 0^\circ$ (a), 30° (b), 90° (c), 180° (d). A similar kind of ISHE signal was observed for all the samples (data not shown). It is observed that the strength of V_{meas} for sample S5 (20-nm-thick Pt) is three times smaller than that of sample S1 (3-nm-thick Pt). This is consistent with the fact that the ISHE voltage is inversely proportional to the conductivity and thickness of the HM layer²⁶.

For the separation of the spin pumping contribution from V_{meas} by excluding other spurious effects, V_{meas} versus H plots for samples S1 (Fig. 3) and S5 (Fig. 4) were fitted with the Lorentzian equation²⁷, which is given by:

$$V_{meas} = V_{sym} \frac{(\Delta H)^2}{(H - H_r)^2 + (\Delta H)^2} + V_{asym} \frac{2\Delta H(H - H_r)}{(H - H_r)^2 + (\Delta H)^2}, \quad (7)$$

where V_{sym} and V_{asym} are the symmetric and antisymmetric components, respectively. Solid lines are the fits to the experimental data. V_{sym} contains a major contribution from spin pumping and minor contributions from the AHE and AMR effects. The AHE contribution is zero here if the rf field and H are perpendicular to each other, which is the case in our measurement. The AHE and AMR are the major contributions in the V_{asym} component. Figures 3 and 4 also show the plots of V_{sym} (dashed line) and V_{asym} (dotted line) separately for samples S1 and S5, respectively.

In-plane angle-dependent measurements of V_{meas} were performed at intervals of 2° to quantify spin pumping and other spin rectification contributions (Fig. 5a, b for sample S1 and Fig. 5c, d for sample S5). This is a well-established method to decouple the individual components from the measured voltage^{25,28,29}. The model given by Harder et al.³⁰ considered the rectification effects, i.e., parallel AMR ($V_{asym/sym}^{AMR\parallel}$) and perpendicular AMR ($V_{asym/sym}^{AMR\perp}$), to



the applied rf field and the AHE contribution due to the FM layer. The relation between the measured voltage and those rectification effects is as follows²⁸:

$$V_{\text{asym}} = V_{\text{AHE}} \cos(\phi + \phi_0) \sin\theta + V_{\text{asym}}^{\text{AMR}\perp} \cos 2(\phi + \phi_0) \cos(\phi + \phi_0) + V_{\text{asym}}^{\text{AMR}\parallel} \sin 2(\phi + \phi_0) \cos(\phi + \phi_0), \quad (8)$$

$$V_{\text{sym}} = V_{\text{sp}} \cos^3(\phi + \phi_0) + V_{\text{AHE}} \cos(\phi + \phi_0) \cos\theta + V_{\text{sym}}^{\text{AMR}\perp} \cos 2(\phi + \phi_0) \cos(\phi + \phi_0) + V_{\text{sym}}^{\text{AMR}\parallel} \sin 2(\phi + \phi_0) \cos(\phi + \phi_0). \quad (9)$$

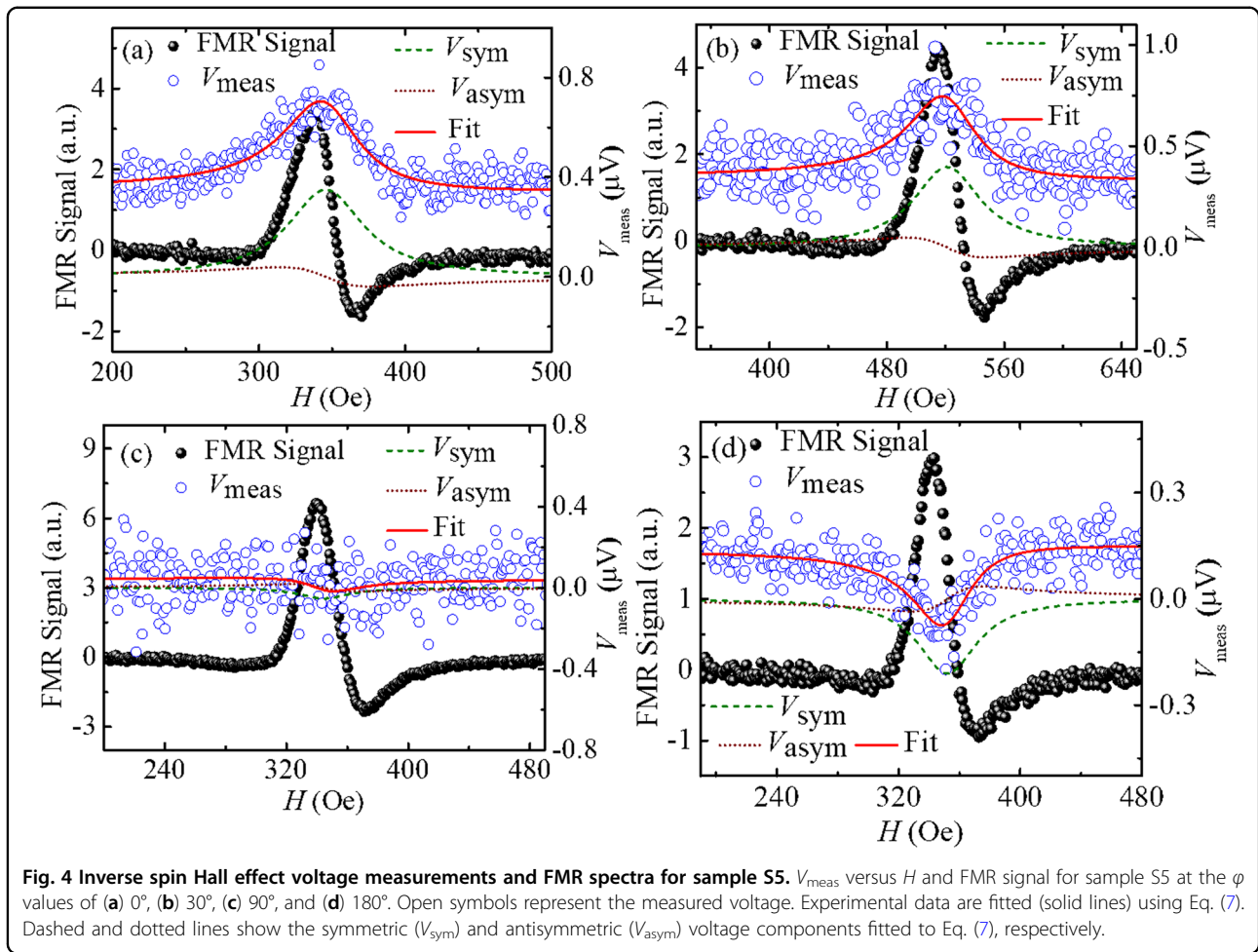
V_{AHE} and V_{sp} correspond to the AHE voltage and the spin pumping contributions, respectively. In addition, θ is the angle between the applied H and the rf magnetic field, which is always perpendicular in the present measurement. The extra factor ϕ_0 is taken to incorporate the misalignment of sample positioning in defining the θ value during the measurement. The detailed fits

with and without incorporation of a small offset in the θ value are shown in Supplementary Figs. A4 and A5 in the Supplementary Information. Further, the AMR contribution can also be quantified by the following formula²⁸:

$$V_{\text{AMR}} = \sqrt{\left(V_{\text{Asym}}^{\text{AMR}\perp,\parallel}\right)^2 + \left(V_{\text{sym}}^{\text{AMR}\perp,\parallel}\right)^2}. \quad (10)$$

Here, $V_{\text{Asym}}^{\text{AMR}\perp,\parallel}$ and $V_{\text{sym}}^{\text{AMR}\perp,\parallel}$ are evaluated from the in-plane angle-dependent V_{meas} measurements by fitting those values by Eqs (8) and (9), respectively. The extracted values of the various components are listed in Table 3.

It is observed that V_{sp} dominates over other unwanted spin rectification effects in all the samples (see Supplementary Fig. A6 in Supplementary Information). However, the magnitude of the AHE is comparable to that of spin pumping, which is decreased by one order of magnitude for thicker Pt samples. This may be due to the increase in conduction of the Pt layer caused by the increase in its thickness. It is well-known that the AHE depends primarily on the magnetization of the sample due to the Berry



curvature of the FM³¹. The AHE contribution is an intrinsic property of the FM layer. Co-based FM materials are always a potential candidate for AHE phenomena^{32,33}. The saturation magnetization measurements of all the samples indicated the presence of MPE in the Pt (see Supplementary Fig. A7 and description in Supplementary Information) or dead layer formation at the interface, which may result in a decrease in the V_{AHE} contribution as the Pt thickness increases from 3 to 20 nm. However, the AMR values are of a similar order in all the samples. The finite AMR contribution indicates that the samples are anisotropic in nature. A positive value of V_{sp} indicates a positive spin Hall angle in Pt, which is consistent with the literature²⁶.

The lowest α in S2 shows the maximum spin pumping voltage (V_{sp}) because of the smooth interface between CFMS/Pt. V_{sp} is dominated by the conductivity of Pt for thicker Pt samples. Thus, V_{sp} decreases with increasing t_{Pt} .

Figure 6a shows the relationship between effective spin mixing conductance $g_{\text{eff}}^{\uparrow\downarrow}$ and Pt thickness, while Fig. 6b represents the Pt thickness dependence of the spin Hall

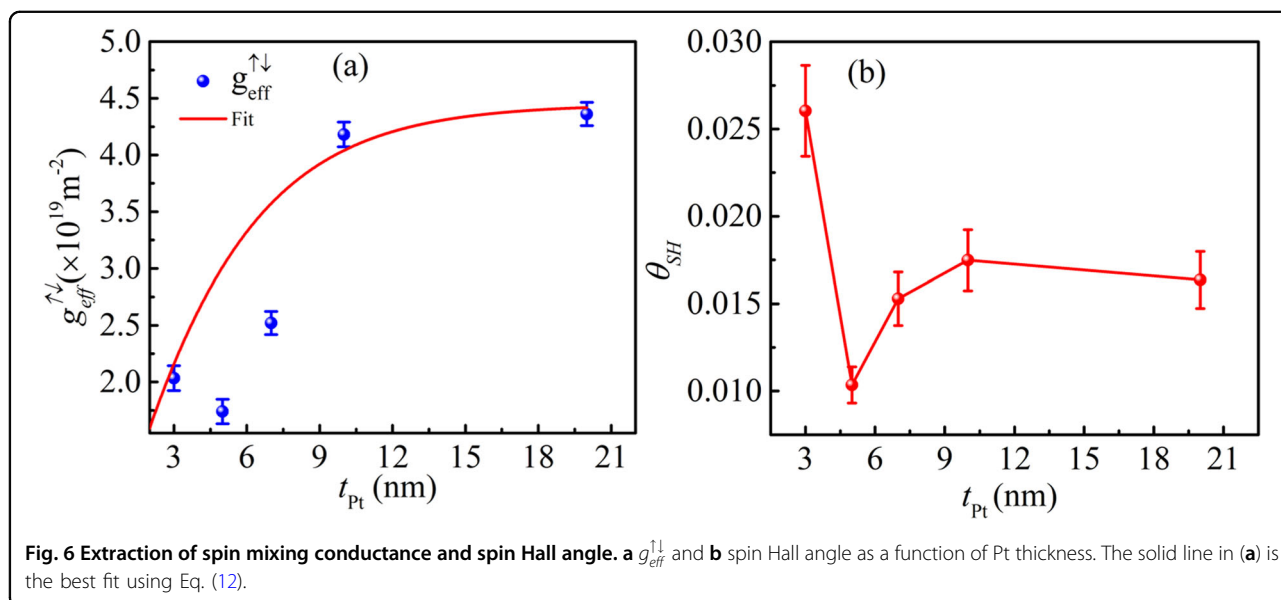
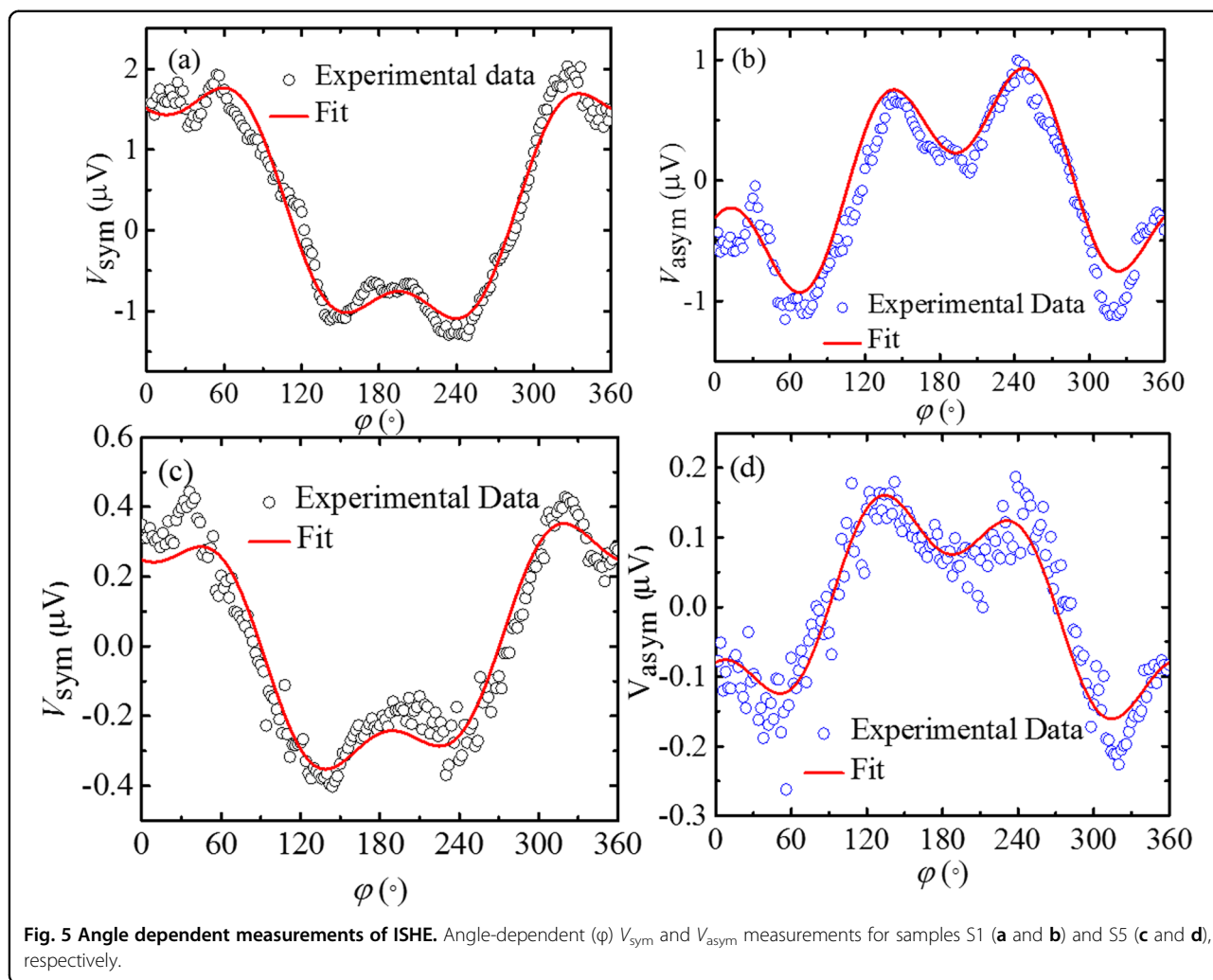
angle. Here, $g_{\text{eff}}^{\uparrow\downarrow}$ was calculated by the following expression using a damping constant²:

$$g_{\text{eff}}^{\uparrow\downarrow} = \frac{\Delta\alpha 4\pi M_S t_{\text{CFMS}}}{g\mu_B}, \quad (11)$$

where $\Delta\alpha$, t_{CFMS} , μ_B , and g are the changes in α due to spin pumping, the thickness of the CFMS layer, the Bohr magneton, and the Lande g -factor (2.1), respectively. To calculate $g_r^{\uparrow\downarrow}$, we considered two models based on spin memory loss (SML) and spin backflow (SBF). The value of $g_r^{\uparrow\downarrow}$ is found to be negative using the SBF model, which is unphysical. This is discussed in detail later. SML is due mainly to interfacial roughness and disorder³⁴. In this model, the effective spin mixing conductance is given by the following equation³⁴:

$$g_{\text{eff}}^{\uparrow\downarrow} = g_r^{\uparrow\downarrow} \frac{r_{\text{sl}} \cosh(\delta) + r_{\text{sl}}^\infty \coth\left(\frac{t_{\text{Pt}}}{\lambda_{\text{Pt}}}\right) \sinh(\delta)}{r_{\text{sl}} \left[1 + 0.5 \sqrt{\frac{3}{\epsilon}} \coth\left(\frac{t_{\text{Pt}}}{\lambda_{\text{Pt}}}\right) \right] \cosh(\delta) + r_{\text{sl}}^\infty \coth\left(\frac{t_{\text{Pt}}}{\lambda_{\text{Pt}}}\right) + 0.5 \frac{r_{\text{sl}}^2}{r_{\text{sl}}^\infty} \sqrt{\frac{3}{\epsilon}} \sinh(\delta)}, \quad (12)$$

where ϵ is the ratio of the spin conserved to spin-flip relaxation times. Based on ref. ³³, we set $\epsilon = 0.1$ for the



present Pt. In addition, r_{sI} , r_{sN}^∞ , δ , and λ_{Pt} are the interfacial spin resistance, Pt spin resistance, spin-flip parameter for the CFMS/Pt interface, and spin diffusion length in Pt, respectively. Figure 6a shows the fitting (solid line) of the data of $g_{eff}^{\uparrow\downarrow}$ using Eq. (12). The fitting gives the values of $\lambda_{Pt} = 7.5 \pm 0.5$ nm, $g_r^{\uparrow\downarrow} = 1.70 \pm 0.03 \times 10^{20}$ m⁻², and $\delta = 0.1$. It is noted here that due to the interdependency of the parameters, we changed each parameter one by one to reach the convergence of the fit. We have varied different values of $g_r^{\uparrow\downarrow}$ in order to obtain the best fit (see Supplementary Fig. A8 in Supplementary Information). We observed that only for $g_r^{\uparrow\downarrow} = 1.7 \times 10^{20}$ m⁻² does the best fit pass through three data points, while the other fits are far from the data points. Therefore, we concluded that this is the best fit.

The values of r_{sI} and r_{sN}^∞ are 0.85 f Ω m² and 0.58 f Ω m², respectively, which are similar to the reported values for Co/Pt systems³⁴. In the CFMS/Pt system, the SML probability ($[1 - \exp(-\delta)] \times 100$) is found to be 9.5%. This implies that the disorder at the interfaces is small since spin depolarization is caused mainly by disorder at the interfaces. The r_{sI} is given by $\frac{r_b}{\delta}$, where r_b is the interface resistance. This indicates that most of the spin current flows through the interface compared to the bulk SOC of the Pt if the SML probability is large. However, in our case, the SML probability is very small (9.5%), which means that most of the spin current is dissipated through the bulk SOC of the Pt, which produces a charge current and hence creates V_{ISHE} . It is mentioned here that such high values of $g_r^{\uparrow\downarrow}$ and $g_{eff}^{\uparrow\downarrow}$ can be due to (1) higher interface spin mixing conductance than Sharvin conductance of Pt, (2) SML at the interface and alloying at the interface of the FM/Pt layer, (3) SBF, and (4) overestimation due to two-magnon scattering (TMS). The spin mixing conductance cannot be higher than the Sharvin conductance of Pt. Further, it is observed that the SML probability is very small (9.5%), which normally comes from interface disorder or alloying. Therefore, SML cannot be the primary reason for observing such a high value of $g_r^{\uparrow\downarrow}$ and $g_{eff}^{\uparrow\downarrow}$. To understand the

role of SBF, we considered the SBF model to evaluate spin mixing conductance using the following equation²:

$$g_r^{\uparrow\downarrow} = \frac{\frac{g_{eff}^{\uparrow\downarrow}}{2\rho_{Pt}\lambda_{Pt}}}{\frac{h}{2e^2\rho_{Pt}\lambda_{Pt}} - g_{eff}^{\uparrow\downarrow} \coth\left(\frac{t_{Pt}}{\lambda_{Pt}}\right)}, \quad (13)$$

where ρ_{Pt} is the resistivity of the Pt layer, which is 2.3×10^{-7} Ω m. The evaluated values of $g_r^{\uparrow\downarrow}$ are found to be negative, which is unphysical. Therefore, it can be concluded that the SBF model is not applicable in our samples and cannot be the reason for the high spin mixing conductance. Further, in order to separate the contribution of TMS in our samples, we performed angle-dependent damping constant measurements in the range of 0 to 180° at intervals of 10° for samples S5 and S6. TMS generally comes from the defects and imperfections present in thin films. If thin films are well ordered, the scattering intensity should follow the symmetry present in the thin films. Because our CFMS thin films are epitaxial and have cubic magnetic anisotropy, the damping constant is symmetric with respect to crystallographic directions. Due to the epitaxial nature of our CFMS thin films, angle-dependent damping analysis gives the opportunity to separate TMS contributions. Conca et al.³⁵ used this methodology with epitaxial Fe/Al, Fe/Pt, and Fe/MgO layers. We chose sample S5 since the interface roughness is highest among the samples; if there is any interface contribution, it is expected to be higher in sample S5. Figure 7a, b shows the angle-dependent damping constant for samples S6 and S5, respectively, revealing the anisotropy in the damping constant. We followed the model given by Arias et al.³⁶, which was also used by Conca et al.³⁵. It can be written as

$$\alpha_{2M} = \sum_{x_i} \Gamma_{x_i} f(\varphi - \varphi_{x_i}), \quad (14)$$

where Γ_{x_i} is the contribution of TMS along the in-plane crystallographic direction x_i . The function $f(\varphi - \varphi_{x_i})$ is

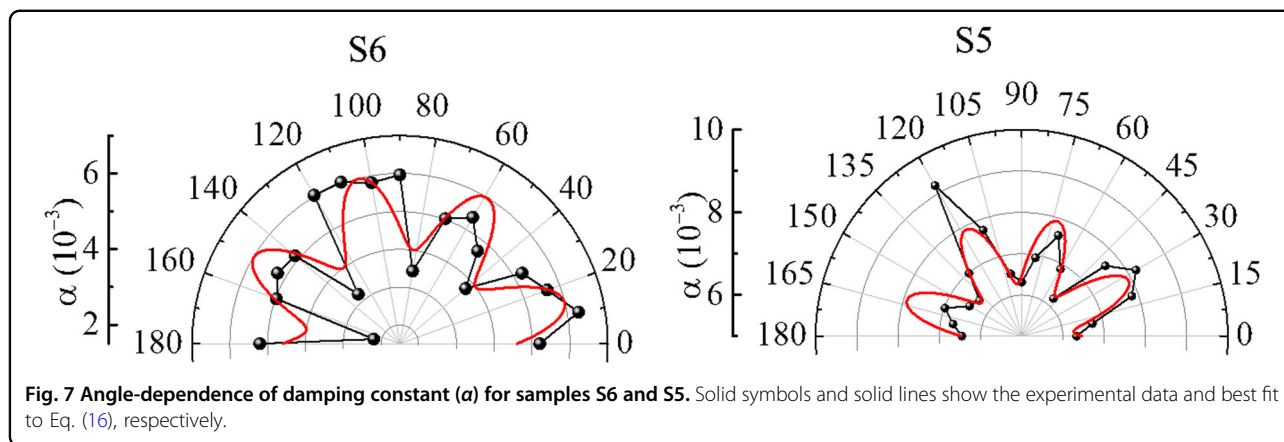


Fig. 7 Angle-dependence of damping constant (α) for samples S6 and S5. Solid symbols and solid lines show the experimental data and best fit to Eq. (16), respectively.

the ansatz and can be written as:

$$f(\varphi - \varphi_{x_i}) = \cos^2(4\varphi - \varphi_{[100]}). \quad (15)$$

Therefore, the effective damping can be written as

$$\alpha = \alpha_{iso} + \alpha_{2M} = \alpha_{iso} + \Gamma_{2M} \cos^2(4\varphi - \varphi_{[100]}), \quad (16)$$

where α_{iso} is the total damping due to Gilbert damping, spin pumping, and magnetic proximity effect. Γ_{2M} represents the strength of the TMS contribution.

We fitted the experimental data (solid symbols) to Eq. (16) (solid line), as shown in Fig. 7a, b, for samples S6 and S5, respectively. The fitting parameters are listed in Table 4. The values of Γ_{2M} are found to be 0.00170 ± 0.00057 and 0.00165 ± 0.00035 for samples S6 and S5, respectively. It is inferred that the strength of the TMS contribution is similar in the single CFMS film (S6) and the bilayer CFMS/Pt sample (S5). Because $g_{eff}^{\uparrow\downarrow}$ is directly proportional to $\Delta\alpha$, it does not affect the calculations of $g_{eff}^{\uparrow\downarrow}$ or $g_r^{\uparrow\downarrow}$. For example, the value of $\Delta\alpha$ is evaluated to be 0.00382 after removing the TMS contribution compared to 0.00386 considering the TMS contribution. The values of $g_{eff}^{\uparrow\downarrow}$ are $4.1 \times 10^{19} \text{ m}^{-2}$ and $4.3 \times 10^{19} \text{ m}^{-2}$ for sample S5 without and with TMS contributions, respectively. Hence, we concluded that the TMS contribution comes from the CFMS layer, not from the interface of the CFMS/Pt layer. This means that TMS is not the reason for observing such a high value of spin mixing conductance. Therefore, the effective value of α , as mentioned in Eq. (6), may have TMS but it cannot have any effect on the evaluation of $g_{eff}^{\uparrow\downarrow}$.

Table 3 Fitted parameters from φ -dependent voltage measurements for all five samples.

Sample	$V_{sp} \text{ (V)} \times 10^{-6}$	$V_{AHE} \text{ (V)} \times 10^{-6}$	$V_{AMR}^{\perp} \text{ (V)} \times 10^{-6}$	$V_{AMR}^{\parallel} \text{ (V)} \times 10^{-6}$
S1	3.93 ± 0.05	-1.14 ± 0.03	2.97 ± 0.06	0.16 ± 0.03
S2	5.41 ± 0.16	-1.28 ± 0.04	3.14 ± 0.18	0.14 ± 0.04
S3	2.88 ± 0.06	-0.78 ± 0.02	1.54 ± 0.07	0.09 ± 0.02
S4	3.26 ± 0.05	-0.67 ± 0.05	2.28 ± 0.06	0.14 ± 0.03
S5	0.89 ± 0.02	-0.64 ± 0.01	0.67 ± 0.02	0.05 ± 0.01

Table 4 Fitting parameters of angle-dependent damping constant data to Eq. (16) for samples S5 and S6.

Sample	$\alpha_{iso} \times 10^{-3}$	$\Gamma_{2M} \times 10^{-3}$	$\Delta\alpha \times 10^{-3}$ with TMS	$\Delta\alpha \times 10^{-3}$ without TMS
S6	3.14 ± 0.34	1.70 ± 0.57	–	–
S5	6.96 ± 0.21	1.65 ± 0.35	3.82 ± 0.55	3.86 ± 0.2

after subtraction of α from a single CFMS layer. From the above, one may infer that the low damping, epitaxial nature, and high spin polarization of the CFMS layer could be the primary sources for observing this high value of $g_{eff}^{\uparrow\downarrow}$.

Further, we compared the $g_r^{\uparrow\downarrow}$ and $g_{eff}^{\uparrow\downarrow}$ values evaluated in this work to the literature for various FM/HM systems in Table 5. It can be observed that the values of $g_r^{\uparrow\downarrow}$ and $g_{eff}^{\uparrow\downarrow}$ are higher than the available literature values for systems with Pt. In addition, it should be noted here that the values of $g_r^{\uparrow\downarrow}$ and $g_{eff}^{\uparrow\downarrow}$ are large compared to those of other reported low-damping systems, viz. $\text{Y}_3\text{Fe}_5\text{O}_{12}/\text{Pt}$, CoFeB/Pt , and $\text{Co}_2\text{MnSi}/\text{Pt}$ ^{37,38}. Therefore, the CFMS/Pt system can be a potential system for spin-transfer torque and logic devices. In addition to $g_r^{\uparrow\downarrow}$, spin interface transparency (T) is another parameter that is useful for spin-orbit torque-based devices. The value of T is affected by the electronic structure matching of the FM and HM layers. We used the following expression to calculate T ³⁹:

$$T = \frac{g_r^{\uparrow\downarrow} \tanh\left(\frac{t_{Pt}}{2\lambda_{Pt}}\right)}{g_r^{\uparrow\downarrow} \coth\left(\frac{t_{Pt}}{\lambda_{Pt}}\right) + \frac{h\sigma_{Pt}}{2e^2\lambda_{Pt}}}, \quad (17)$$

where σ_{Pt} is the conductivity of Pt layer. For $t_{Pt} = 20 \text{ nm}$, T is calculated to be 0.83 ± 0.02 by Eq. (17), which is much higher than the values reported in the literature for NiFe/Pt and Co/Pt systems³⁹. Further, it is also higher than the recently developed low-damping $\text{Co}_2\text{FeAl}/\text{Ta}$ layer system (68%)⁴⁰. We also calculated θ_{SH} for Pt using the following expression²:

$$|\vec{J}_s| \approx \left(\frac{g_{eff}^{\uparrow\downarrow} \hbar}{8\pi}\right) \left(\frac{\mu_0 h_f \gamma}{\alpha}\right)^2 \times \left[\frac{\mu_0 M_S \gamma + \sqrt{(\mu_0 M_S \gamma)^2 + 16(\pi f)^2}}{(\mu_0 M_S \gamma)^2 + 16(\pi f)^2}\right] \left(\frac{2e}{\hbar}\right), \quad (18)$$

$$V_{ISHE} = \left(\frac{w_y}{\sigma_{FM} t_{FM} + \sigma_{Pt} t_{Pt}}\right) \times \theta_{SH} \lambda_{Pt} \tanh\left(\frac{t_{Pt}}{2\lambda_{Pt}}\right) |\vec{J}_s|. \quad (19)$$

The resistivity (ρ) of the samples was measured using the four-probe technique, and ρ_{Pt} and ρ_{CFMS} were found to be $2.3 \times 10^{-7} \Omega\text{-m}$ and $1.7 \times 10^{-6} \Omega\text{-m}$, respectively.

Table 5 Spin diffusion length (λ_{Pt}), spin mixing conductance ($g_r^{\uparrow\downarrow}$), and effective mixing conductance ($g_{eff}^{\uparrow\downarrow}$) obtained from the literature and in this work.

Layer structure	λ_{Pt} (nm)	$g_r^{\uparrow\downarrow}$ (m^{-2})	$g_{eff}^{\uparrow\downarrow}$ (m^{-2})
NiFe/Pt ⁴¹	7.7	1.13×10^{20}	3.02×10^{19}
NiFe/Pt ⁵	8.4	2.53×10^{19}	2.50×10^{19}
CoFe/Pt ⁵	7.6	2.65×10^{19}	2.50×10^{19}
Co/Pt ⁵	8.0	1.42×10^{19}	1.40×10^{19}
Y ₃ Fe ₅ O ₁₂ /Pt ³⁷	7.3	3.90×10^{18}	6.90×10^{18}
CoFeB/Pt ³⁸	1.7	3.90×10^{19}	3.90×10^{19}
Co ₂ MnSi/Pt ⁹	10.0		1.50×10^{19}
Co ₂ Fe _{0.4} Mn _{0.6} Si/Pt (this work)	7.5	1.70×10^{20}	4.01×10^{19}

Here, σ corresponds to the conductivity of the individual layers.

The rf field ($\mu_0 h_{rf}$) and CPW transmission linewidth (w_p) for our setup are 0.5 Oe (at +15 dBm rf power) and 200 μ m, respectively. The obtained values of θ_{SH} are plotted in Fig. 6b. The values of θ_{SH} are comparable to the literature values⁴¹. In our case, we observe a higher SHA value for sample S1 than for sample S5. This may be due to the higher resistivity of the 3-nm Pt layers, which is consistent with the results obtained by Liu et al.⁴².

Further, we also determined the power dependence of the V_{ISHE} measurements (Supplementary Fig. A9, Supplementary Information). We observed a linear dependence of V_{ISHE} , which confirmed spin pumping at the CFMS/Pt interface.

Conclusion

We observed a strong dependency of the spin pumping voltage on the thickness of Pt. The spin pumping voltage was decreased when the thickness of Pt was increased, which may be due to the increase in conductivity of Pt with increasing thickness. The presence of substantial spin pumping maintains the damping constant values on the order of $\sim 10^{-3}$. The $g_r^{\uparrow\downarrow}$ was obtained to be $1.70 \times 10^{20} m^{-2}$, higher than those for the other reported FM/Pt systems. We also performed angle-dependent damping constant measurements to quantify TMS contributions. We found that TMS in CFMS/Pt is not significant and does not affect the obtained high value of $g_r^{\uparrow\downarrow}$. In addition, we observed the highest spin interface transparency (83%) of any FM/Pt system. Low magnetic damping and a large value of $g_r^{\uparrow\downarrow}$ with high interface transparency make the CFMS/Pt system a potential candidate for spintronic applications.

Acknowledgements

The authors acknowledge DAE and DST, Government of India, for financial support of the experimental facilities. B.B.S. acknowledges DST for INSPIRE faculty fellowship. K.R. and P.G. thank CSIR and UGC for their JRF fellowships,

respectively. S.B. acknowledges an ICC-IMR fellowship to visit IMR, Tohoku University, for this collaborative work to prepare the thin films.

Author details

¹Laboratory for Nanomagnetism and Magnetic Materials (LNMM), School of Physical Sciences, National Institute of Science Education and Research (NISER), HBNI, Jatni, Odisha, India. ²Institute for Materials Research, Tohoku University, Sendai, Japan. ³Center for Spintronics Research Network, Tohoku University, Sendai, Japan. ⁴Center for Science and Innovation in Spintronics, Core Research Cluster, Tohoku University, Sendai, Japan

Author contributions

S.B. conceived the idea. B.B.S., S.B., and T.S. designed the experiment. Sample preparation and RHEED observation were performed by T.S. and S.B. Spin pumping and ISHE measurements were performed by B.B.S. and K.R. Resistivity measurements were performed by B.B.S., K.R. and P.G. SQUID measurements were performed by P.G. and B.B.S. Data analysis and discussion were conducted by B.B.S., K.R., S.B., and T.S. Spin mixing conductance and spin transparency analysis were performed by B.B.S. This paper was written by B.B.S., K.R., and S.B. All authors contributed to the paper corrections.

Conflict of interest

The authors declare that they have no conflict of interest.

Publisher's note

Springer Nature remains neutral with regard to jurisdictional claims in published maps and institutional affiliations.

Supplementary information is available for this paper at <https://doi.org/10.1038/s41427-020-00268-7>.

Received: 11 March 2020 Revised: 5 October 2020 Accepted: 15 October 2020.

Published online: 22 January 2021

References

- Bader, S. D. & Parkin, S. S. P. Spintronics. *Annu. Rev. Condens. Matter Phys.* **1**, 71–88 (2010).
- Tserkovnyak, Y., Brataas, A., Bauer, G. E. W. & Halperin, B. I. Nonlocal magnetization dynamics in ferromagnetic heterostructures. *Rev. Mod. Phys.* **77**, 1375–1421 (2005).
- Avci, C. O. et al. Unidirectional spin Hall magnetoresistance in ferromagnet/nonmagnetic metal bilayers. *Nat. Phys.* **11**, 570–575 (2015).
- Sánchez, J. C. R. et al. Spin-to-charge conversion using Rashba coupling at the interface between non-magnetic materials. *Nat. Commun.* **4**, 2944 (2013).
- Tao, X. et al. Self-consistent determination of spin Hall angle and spin diffusion length in Pt and Pd: the role of the interface spin loss. *Sci. Adv.* **4**, eaat1670 (2018).
- Uchida, K. et al. Observation of the spin Seebeck effect. *Nature* **455**, 778–781 (2008).
- Saitoh, E., Ueda, M., Miyajima, H. & Tatara, G. Conversion of spin current into charge current at room temperature: inverse spin-Hall effect. *Appl. Phys. Lett.* **88**, 182509 (2006).
- Tserkovnyak, Y., Brataas, A. & Bauer, G. E. W. Enhanced Gilbert damping in thin ferromagnetic films. *Phys. Rev. Lett.* **88**, 117601 (2002).
- Chudo, H. et al. Spin pumping efficiency from half metallic Co₂MnSi. *J. Appl. Phys.* **109**, 073915 (2011).
- Demidov, V. E. et al. Magnetization oscillations and waves driven by pure spin currents. *Phys. Rep.* **673**, 1–31 (2017).
- Mizukami, S., Ando, Y. & Miyazaki, T. Effect of spin diffusion on Gilbert damping for a very thin permalloy layer in Cu/permalloy/Cu/Pt films. *Phys. Rev. B* **66**, 104413 (2002).
- Miao, B. F., Huang, S. Y., Qu, D. & Chien, C. L. Inverse Spin Hall effect in a ferromagnetic metal. *Phys. Rev. Lett.* **111**, 066602 (2013).
- Chen, L., Ikeda, S., Matsukura, F. & Ohno, H. DC voltages in Py and Py/Pt under ferromagnetic resonance. *Appl. Phys. Express* **7**, 013002 (2013).
- Kim, S.-I., Seo, M.-S., Choi, Y. S. & Park, S.-Y. Irreversible magnetic-field dependence of ferromagnetic resonance and inverse spin Hall effect voltage in CoFeB/Pt bilayer. *J. Magn. Magn. Mater.* **421**, 189–193 (2017).

15. Cecot, M. et al. Influence of intermixing at the Ta/CoFeB interface on spin Hall angle in Ta/CoFeB/MgO heterostructures. *Sci. Rep.* **7**, 1–11 (2017).
16. Gościańska, I. & Dubowik, J. Inverse Spin Hall Effect by spin-pumping in Co₂Cr_{1-x}(0.4)Fe_{1-x}(0.6)Al/Pt structures. *Acta Phys. Polonica A* **118**, 851–853 (2010).
17. Hirohata, A. & Takanashi, K. Future perspectives for spintronic devices. *J. Phys. D: Appl. Phys.* **47**, 193001 (2014).
18. Pan, S., Seki, T., Takanashi, K. & Barman, A. Role of the Cr buffer layer in the thickness-dependent ultrafast magnetization dynamics of Co₂Fe_{0.4}Mn_{0.6} Si Heusler alloy thin films. *Phys. Rev. Appl.* **7**, 064012 (2017).
19. Pan, S., Seki, T., Takanashi, K. & Barman, A. Ultrafast demagnetization mechanism in half-metallic Heusler alloy thin films controlled by the Fermi level. *Phys. Rev. B* **101**, 224412 (2020).
20. NanOsc A. B. *NanOsc AB* <http://www.nanosc.se/>.
21. Singh, B. B., Jena, S. K. & Bedanta, S. Study of spin pumping in Co thin film vis-à-vis seed and capping layers using ferromagnetic resonance spectroscopy. *J. Phys. D: Appl. Phys.* **50**, 345001 (2017).
22. Singh, B. B. et al. Inverse spin Hall effect in electron beam evaporated topological insulator Bi₂Se₃ thin film. *Phys. Status Solidi (RRL) – Rapid Res. Lett.* **13**, 1800492 (2019).
23. Kittel, C. On the theory of ferromagnetic resonance absorption. *Phys. Rev.* **73**, 155–161 (1948).
24. Heinrich, B., Cochran, J. F. & Hasegawa, R. FMR linebroadening in metals due to two-magnon scattering. *J. Appl. Phys.* **57**, 3690–3692 (1985).
25. Conca, A. et al. Study of fully epitaxial Fe/Pt bilayers for spin pumping by ferromagnetic resonance spectroscopy. *Phys. Rev. B* **93**, 134405 (2016).
26. Ando, K. et al. Inverse spin-Hall effect induced by spin pumping in metallic system. *J. Appl. Phys.* **109**, 103913 (2011).
27. Iguchi, R. & Saitoh, E. Measurement of spin pumping voltage separated from extrinsic microwave effects. *J. Phys. Soc. Jpn.* **86**, 011003 (2016).
28. Conca, A. et al. Lack of correlation between the spin-mixing conductance and the inverse spin Hall effect generated voltages in CoFeB/Pt and CoFeB/Ta bilayers. *Phys. Rev. B* **95**, 174426 (2017).
29. Harder, M., Gui, Y. & Hu, C.-M. Electrical detection of magnetization dynamics via spin rectification effects. *Phys. Rep.* **661**, 1–59 (2016).
30. Harder, M., Cao, Z. X., Gui, Y. S., Fan, X. L. & Hu, C.-M. Analysis of the line shape of electrically detected ferromagnetic resonance. *Phys. Rev. B* **84**, 054423 (2011).
31. Nagaosa, N., Sinova, J., Onoda, S., MacDonald, A. H. & Ong, N. P. Anomalous Hall effect. *Rev. Mod. Phys.* **82**, 1539–1592 (2010).
32. Zhang, W. et al. Determination of the Pt spin diffusion length by spin-pumping and spin Hall effect. *Appl. Phys. Lett.* **103**, 242414 (2013).
33. Zahnd, G. et al. Spin diffusion length and polarization of ferromagnetic metals measured by the spin-absorption technique in lateral spin valves. *Phys. Rev. B* **98**, 174414 (2018).
34. Rojas-Sánchez, J.-C. et al. Spin pumping and inverse spin Hall effect in platinum: the essential role of spin-memory loss at metallic interfaces. *Phys. Rev. Lett.* **112**, 106602 (2014).
35. Conca, A., Keller, S., Schweizer, M. R., Papaioannou, E. T. H. & Hillebrands, B. Separation of the two-magnon scattering contribution to damping for the determination of the spin mixing conductance. *Phys. Rev. B* **98**, 214439 (2018).
36. Arias, R. & Mills, D. L. Extrinsic contributions to the ferromagnetic resonance response of ultrathin films. *Phys. Rev. B* **60**, 7395–7409 (1999).
37. Wang, H. Understanding of Pure Spin Transport in a Broad Range of Y3Fe5O12-Based Heterostructures. PhD, The Ohio State Univ. (2015).
38. Belméguenai, M. et al. Investigation of the annealing temperature dependence of the spin pumping in Co₂₀Fe₆₀B₂₀/Pt systems. *J. Appl. Phys.* **123**, 113905 (2018).
39. Zhang, W. et al. Role of transparency of platinum–ferromagnet interfaces in determining the intrinsic magnitude of the spin Hall effect. *Nat. Phys.* **11**, 496–502 (2015).
40. Akansel, S. et al. Thickness-dependent enhancement of damping in Co₂ FeAl/β-Ta thin films. *Phys. Rev. B* **97**, 134421 (2018).
41. Nakayama, H. et al. Geometry dependence on inverse spin Hall effect induced by spin pumping in Ni₈₁Fe₁₉/Pt films. *Phys. Rev. B* **85**, 144408 (2012).
42. Liu, J., Ohkubo, T., Mitani, S., Hono, K. & Hayashi, M. Correlation between the spin Hall angle and the structural phases of early 5d transition metals. *Appl. Phys. Lett.* **107**, 232408 (2015).